Screening of Six Different Potential HLRW Canister Materials Surrounded by Bentonite

Stephan Kaufhold, PhD
BGR, Bundesanstalt für Geowissenschaften und Rohstoffe
Christoph Kahra, Thomas Hassel
2IW-LUH, Institut für Werkstoffkunde, Leibniz University Hannover
Nicolas Finck
3INE, Institut für Nukleare Entsorgung, Karlsruhe Institute of Technology
Andres Muñoz
4GRS, Gesellschaft für Anlagen und Reaktorsicherheit GmbH

Abstract

Most countries seeking strategies for the disposal of high-level nuclear (HLW) waste envisage the use of metallic containers. In some deep geological repositories, the canister will be in contact with bentonite. Different types of metals were tested so far with ambiguous results. Consistent data are available for copper and carbon steel. Different performances, however, were reported for stainless steel. In the present study six different alloys were tested: three iron-matrix alloys with different carbon contents and grain sizes, a copper-nickel alloy, zirconium, and stainless steel. They were immersed with water saturated bentonite for 10 months at 23°C under anaerobic conditions. Corrosion was assessed gravimetrically and using electron- and X-ray microscopy. Stainless steel did not show any reaction with the bentonite despite its widespread classification as disadvantageous because of its susceptibility for local corrosion at low pH and high Cl- concentrations. Many studies using stainless steel, however, were conducted with simulating bentonite pore waters but without contact with bentonite which meanwhile is known to buffer both pH and redox potential (Eh). The promising results of the stainless-steel corrosion tests in the present study encourage further systematic investigations to improve the predictability of stainless-steel performance as HLW canister material surrounded by bentonite.

KEYWORDS
iron/bentonite interaction, HLRW canister materials, anaerobic metal corrosion

Introduction

Different concepts for the storage of high-level radioactive waste (HLW) worldwide are currently being pondered. Many countries focus on deep geological storage sites (deep geological repositories, DGR) ideally in tight or almost tight rocks in which the HLW will be placed in containers, predominantly manufactured with combinations of different steels and non-ferrous alloys[1,2]. The container represents the most essential barrier for the retention of hazardous constituents (radionuclides) which could be released from the HLW to the biosphere. Depending on the regional varying repository concept and on the host rock properties, different additional barriers may be considered. The metallic canister is expected to isolate the waste in the initial phase of emplacement with the highest level of radioactivity (thermal phase). Therefore, the investigation of the corrosion behavior of candidate container materials under near field conditions is quite significant. Anaerobic conditions are expected to prevail after a short oxic period following the closure of a deposition hole or the entire gallery.

Copper, cast iron, and carbon steel are often considered as a possible canister material. In Finland and Sweden, in which granite formations were selected as a host rock, containers with an outer wall of copper are planned to be used[3]. Because of the typical partly fractured host rocks, bentonite, a highly swelling clay, will be implemented as additional barrier to keep the HLW out of the biosphere. Hence, the Cu canister is put in contact with bentonite. Possible reactions taking place at this interface, therefore, determine the long-term performance of the canister.

Hitherto, no specific reaction of typical bentonite constituents accelerating the corrosion of copper could be identified, except for pyrite (or other sulphides including those possibly produced by microbial activity). As pyrite is present in the bentonite, corrosion of the Cu canister can be triggered by formation of Cu-sulphides[4,5,6,7]. Without pyrite or other sulphides, much less Cu corrosion and no specific reaction is observed.

For iron, on the other hand, a specific reaction with the major bentonite constituent, smectite, was reported. The underlying mechanism(s), however, are still under discussion. After a short oxic period which is difficult to predict with respect to its duration (oxic corrosion is described in detail by Wersin and Kober[8]) anaerobic corrosion prevails. Under anaerobic conditions, hydrogen forms from the cathodic water reduction associated with iron oxidation to ferrous ions, independently from the presence of bentonite. Fe^{2+} forms a Fe-hydroxide-gel (later altering to magnetite[9]) or is incorporated in the bentonite as Fe-silicate. A possible diffusion of Fe^{2+} through the barrier and a subsequent cation exchange with the initially present interlayer cations was also argued[10,11,12]) but Fe^{2+}, on the other hand, is also known to form stable surfaces complexes on smectite[13]. An increase of the iron concentration was observed only in the proximity of the canister in large scale tests (e.g., Febex [14]) for which highly compacted bentonite blocks were used. This suggests that the Fe^{2+} does not easily migrate through the barrier. Mineralogical analyses of corrosion products obtained from both in-situ and laboratory experiments indicate that different iron minerals can form in the vicinity of the canister [15, 16, 17, 18]. The nature of corrosion products may appear as relevant in the case it constitutes an active part of the corrosion dynamics at the metal-bentonite interface. Rather consistent data of long-term corrosion rates ranging from 2 – 5 µm/a were reported for diverse Fe-based materials[19,20,21]. Initially a much larger rate is observed in corrosion tests, attaining a constant value after some years. King[22] and Hesketh et al.[23] reported long term corrosion rates of carbon steel even below 1 µm/a. Differences in reported corrosion rates could in part be explained by the layer charge density of the smectites in the bentonites[24] which in turn affects their characteristic redox potentials. Thus, it is possible that anaerobic corrosion is driven by the redox milieu generated by the bentonites. As a consequence, corrosion tests conducted in solutions without the presence of bentonite are not representative of the real system because bentonite is not inert as commonly assumed. The structural Fe^{3+} of the smectites acts as an electron acceptor thus buffering the Eh which is the prerequisite for proceeding corrosion. Without the presence of bentonite as an Eh buffer, the redox potential would shift rapidly towards lower values attaining a stable value after an initial corrosion phase in which hydrogen and ferrous hydroxide (later magnetite) are produced. The use of stainless steel as a material for canisters can considerably mitigate the corrosion issue. Its corrosion resistance lies on the chemical and possibly also mechanical properties of the naturally grown passive layer which results from the chemical composition of the alloys, especially Cr and Mo contents[25]. Stainless steels, however, are susceptible to localized corrosion (e.g., pitting) because of the breakdown of the passive film caused e.g., by aggressive halide anions[26]. The pitting resistance equivalent number (PREN), widely used to categorize stainless steels, is given by PREN = %Cr + 3.3 (%Mo + 0.5%W) + 16%N[27]. In direct correlation to corrosion resistance, the statement applies that the higher the PREN value, the higher the corrosion resistance of the steel, which can be easily proven by electrochemical considerations[28].

King[22] provided a discussion about the use of stainless steel among other metals/alloys as materials for HLW containers. Oxygen is forecasted to vanish inside the DGR in the long-term. The performance of stainless steel under anaerobic conditions is still not clear. One of the latest studies concerning this issue was provided by Payer et al.[29]. They evaluated the performance of a canister of NiCrMo-alloy 625 (UNS N06625) with a casing of stainless steel API-5CT L80 in a deep horizontal drillhole using corrosion data compilated from the literature, mostly from the Yucca Mountain research. This study forecasts a long-life outstanding corrosion resistance of the container alloy, partly benefited by the consumption of oxygen by corrosion of the casting steel. Moreover, Stoulil et al.[30] studied the corrosion of stainless steel 316L and of duplex 2205 (UNS S32205) in Czech synthetic bentonite pore water at temperatures between 40°C and 90°C. They found that a localized attack arises only in the presence of bentonite at 90°C, which was ascribed to the adsorption of bentonite hindering the re-passivation of metastable pits.

In the frame of the MaCoTe project, an in-situ anaerobic corrosion long-term experiment, Reddy et al.[31] compared the corrosion rates of stainless steel with carbon steel and various types of copper. While no detectable corrosion was assessed

for the duplex stainless steel 2205, after 13 months values of 2 µm/a and 0.2 µm/a were measured for carbon steel ASTM A694-08F65 and copper, respectively.

Similarly, Gaudin et al.[32] found no evidence of corrosion of stainless steels 309S and 316L after 6 years long in-situ experiments performed in contact with Tournemire argillite, where the presence of oxygen could not be excluded. This contrasted with carbon steel, where a marked crevice and pitting corrosion with a strong interaction of corrosion products with the argillite was observed. More recently, Necib et al.[33] corroborated the absence of significant corrosion of 316L after several years of contact with clay minerals in in situ experiments under anoxic conditions in Opalinus Clay.

There is valuable evidence for considering stainless steel as a convenient material selection, because it shows a stable passive state in contact with bentonite as long as the passive layer is intact. In this context, an experimental approach for the screening of the performance of a wide spectrum of materials is presented. The present study was conducted to compare different metals/alloys which were and are considered as suitable construction materials in the frame of HLW repository research.

Six different metals were selected for the screening experiment: a fine-grained construction steel (1.6210; abbreviation this study: FGCS), a spheroidal graphite cast iron (0.7040 or EN GJS 400 15; abbreviation this study: SGCI), an austenitic stainless steel (1.4833 or AISI 309 S; abbreviation this study: ASS), a spring steel (1.5026; abbreviation this study: SS), a CuNi alloy (2.0882 or C71500; abbreviation this study: CNA), and a zirconium alloy (Zr702 or UNS R60702; abbreviation this study: ZA).

Among the reported international designs, the POLLUX® cask was originally developed for the final disposal of heat generating radioactive waste in salt rock in Germany. It was then modified to adapt it for the storage in clay-based repositories[34]. Such casks consist of an inner cask made of fine structural steel (1.6210; corresponding to FGCS in the present study). In some countries (e.g., Sweden, Finland, Canada), the container designs are provided with an outer copper shell to guarantee a very low corrosion rate in water in the absence of sulphides. The alloying of copper with nickel increases its corrosion resistance and mechanical and physical properties. CuNi alloys are the preferred materials for the construction of evaporators and heat exchange tubes and find especially application in marine engineering because of their excellent corrosion behavior in sea water[35]. The alloy C71500 containing ~ 30 mass% Ni was thus selected to explore the effect of Ni addition on the Cu corrosion behavior (corresponding to CNA in the present study). The austenitic stainless steel AISI 309 S (ASS in the present study) is the typical material used to construct flasks containing vitrified waste because its high Cr and Ni contents make this material suited to withstand conditions imposed by pouring the glass melt[36]. This material is presently not considered as candidate to construct waste containers[22], but it was selected to determine the nature of secondary phases that may form following overpack failure. The zirconium alloy Zr702 (ZA in the present study) is used as an analogue of zircalloy, which is applied as nuclear fuel cladding. In this case, there is an interest to obtain information regarding the corrosion behavior in a clay-based repository, following overpack failure. Spring steel (1.5026; corresponding to SS in the present study) has a composition comparable to that of the fine-grained construction steel except for its higher silicon content. Earlier findings suggest that the presence of reactive silica influences the nature of the secondary phases forming during steel corrosion[4]. The spheroidal graphite cast iron (0.7040; corresponding to SGCI in the present study) was selected to investigate a possible role of different C-contents in the Fe-based alloys with respect to the corrosion rate.

The aim of the study was to characterize the different performances of these metals/alloys under realistic conditions (first exposed to oxygen and then stored anaerobically in contact with bentonite and low water contents).

Materials and Methods

Corrosion experiments were performed with a bentonite which among others turned out as relatively corrosive for pure iron[24]. The characterization of this bentonite is provided in Table 1 and the chemical composition of all selected materials is presented in Table 2.

Table 1. Basic bentonite data of the bentonite used for exposition tests[37].

Bentonite Slovakia		B 36	Chemical Composition (XRF)		
BET/SSS			SiO_2	mass%	61.7
SSA	[m2/g]	57	TiO_2	mass%	0.8
soda soluble silica	[mass%]	1.0	Al_2O_3	mass%	17.5
			Fe_2O_3	mass%	8.1
CEC			MnO	mass%	0.1
Na^+	[meq/100g]	0	MgO	mass%	1.6
K^+	[meq/100g]	2	CaO	mass%	1.3
Mg^{2+}	[meq/100g]	17	Na_2O	mass%	0.4
Ca^{2+}	[meq/100g]	36	K_2O	mass%	1.4
CEC	[meq/100g]	53	P_2O_5	mass%	0.1
LCD_{AAM}	[eq/FU]	0.20	(Cl)_SI	mass%	0.0
tet.charge	[%/CEC]	51	LOI_SI	mass%	6.7
			Sum_RF	mass%	100
Mineralogical Composition [37]			**Trace Elements > 20 mg/kg**		
Smectite	[mass%]	**75**	Ba	mg/kg	409
Quartz	[mass%]	11	Ce	mg/kg	57
Cristobalite	[mass%]	3	Co	mg/kg	21
Feldspars	[mass%]	8	Cr	mg/kg	29
Rutile	[mass%]	0	Cu	mg/kg	25
Kaolinite	[mass%]	2	La	mg/kg	38
			Rb	mg/kg	73
LECO			Sr	mg/kg	146
C_{ges}	[mass%]	0.06	V	mg/kg	147
C_{org}	[mass%]	0.06	Zn	mg/kg	98
C_{carb}	[mass%]	0.00	Zr	mg/kg	148
S_{ges}	[mass%]	0.00			

Table 2. Chemical composition of materials selected in this study in mass% as indicated on the inspection certificate (EN 10204/3.1).

Sample		Abbreviation this study	Composition	Fe	C	Si	Cr	Mn	Ni	Cu	Zr	Mo	Hf	others
Zr 7020 *zirconium alloy*	6.0702	**ZA**	[mass%]								97		3	0
EN GJS400 15 *spheroidal graphite cast iron*	0.7040	**SGCI**	[mass%	92	>4.4	2.7	0.0	0.3	0.0	0.0		0.0		< 0.3
56 Si7 *spring steel*	1.5026	**SS**	[mass%	96	0.4	1.8	0.2	0.7	0.2	0.3		0.1		0.2
CuNi30Mn1Fe *CuNi*	2.0822	**CNA**	[mass%	0.1				0.8	31.4	68				0
15 Mn Ni 6-3 *fine grained construction steel*	1.6210	**FGCS**	[mass%	97	0.2	0.3	0.1	1.6	0.7	0.0				0.2
X12CrNi23-13 *austenitic stainless steel*	1.4833	**ASS**	[mass%	62	0.1	0.4	22.5	1.2	13.2	0.2		0.3		0.7

The six different alloys were reacted with 15 g of bentonite B36 each. The bentonite powder was stored in a glovebox for one month to remove residual oxygen. The bentonites were then mixed with 15 mL of deionized and degassed water in 50 mL Teflon vessels and allowed to swell for 24 h. For each type of alloy, a separate vessel was used. In each vessel 20 pellets (diameter 8 mm, height 3 mm) were put into the bentonite gel (in the glove box) ensuring that they were fully covered, did not touch each other, and did not touch the wall of the vessel. The pellets were weighed before using an analytical balance (± 0.1 mg). The total mass varied between 19 and 20 g. After a reaction time of 10 months, the pellets were retrieved from the bentonite gel in a glove box using tweezers and put into 25 mL glass vials filled with 20 mL ethanol. After repeated washing, the pellets were dried in dry nitrogen, taken out of the box, and weighed back outside the glovebox using the same balance as before. Based on the gravimetrically determined mass loss and considering the dimensions and density of the pellets, the corrosion rate in µm/a was calculated.

For scanning electron microscopy (SEM) and X-ray microscopy (XRM) investigations parallel experiments were conducted with smaller pieces of the same materials (1 mm diameter and 1 mm thickness). They were put in 10 mL Teflon vessels containing the same bentonite gel and were treated the same way as the bigger pellets which were used to derive the gravimetrical data. The reason for performing parallel experiments is that gravimetrical data needs higher mass of metal to reduce the weighing error and for electron optical inspection, particularly for the X-ray microscope, using smaller particles leads to higher resolution.

A Zeiss Sigma 300 V P FEG scanning electron microscope operating at 15 kV was used to evaluate samples in the micro scale using the high-vacuum mode. Sputtering the samples was not needed because of sufficient electrical conductivity of the Fe-pellets. The microscope was equipped with the following detectors: Bruker Xflash® 6/60 EDX detector, high-definition backscattered electron detector (HDBSD), secondary electron detector (SE2), variable pressure secondary electron detector (VPSE), and an InLens detector for detection of secondary and backscattered electrons, respectively.

X-ray microscopy and tomography was performed with a Zeiss Xradia 520 Versa (Carl Zeiss AG, Oberkochen, Germany). For the microscopy mode a 4X objective was used. The iron and steel samples were measured with an acceleration voltage of 140 keV and an exposure time of 15 seconds. For the CuNi samples, the exposure time was increased to 20 seconds. For the zirconium samples the acceleration voltage was increased to 160 keV and the exposure time to 25 seconds. 3201 projections were acquired per sample. The spatial voxel size was 0.61 µm x 0.61 µm x 0.61 µm. To obtain the tomography, the cylindrical samples were placed in the beam path and rotated. Projections (two-dimensional images) were acquired at different angles. After measurement, the tomography was built from the projections. Dragonfly 2020 software (ORS, Montréal, Canada) was used to reconstruct the tomography and generate the images.

Results

Table 3 shows the gravimetrically determined corrosion rates of the six different metals in contact with bentonite. Mass

Table 3. Corrosion rates of the six different metals determined gravimetrically.

Sample		Abbreviation this study	Density [g/cm^3]	Δm 10 months [%]	Rate/10M [µm/a]
Zr 7020 *zirconium alloy*	6.0702	**ZA**	6.7	0.0	**0**
EN GJS400 15 *spheroidal graphite cast iron*	0.7040	**SGCI**	7.2	1.6	**9**
56 Si7 *spring steel*	1.5026	**SS**	8.0	2.0	**12**
CuNi30Mn1Fe *CuNi*	2.0822	**CNA**	8.6	0.2	**1**
15 Mn Ni 6-3 *fine grained construction steel*	1.6210	**FGCS**	8.3	1.8	**11**
X12CrNi23-13 *austenitic stainless steel*	1.4833	**ASS**	8.1	0.0	**0**

changes were under the detection limit for zirconium alloy (ZA) and stainless steel 309S (ASS). The corrosion rate of CuNi-alloy (CAN) was about one tenth compared to the iron-based alloys.

SEM pictures of the surfaces of the pellets of the zirconium alloy (ZA) before and after the corrosion test are shown in Fig. 1a and 1b. Before the corrosion test (Fig. 1a) the surface showed a texture characterized by long oriented strips, scratches, and pits of 110 µm which are inherent effects of the material removal by the electrical discharge machining[38,39]. After the corrosion test the original texture is maintained and additional larger irregular pits and cavities can be observed (Fig. 1b). The presence of deposited massive corrosion products cannot be distinguished.

X-ray microscopy pictures of the surface of the pellets of ZA before and after the corrosion tests are shown in Fig. 1c and 1d, respectively. Before corrosion, the surface showed an approximately five µm slightly darker thick outer layer which points to a lower density compared to the pellet. This layer supposedly reflects the rough topography (scratches and pits) of the surface covered with a native oxide. Practically no changes of this layer can be discerned after corrosion.

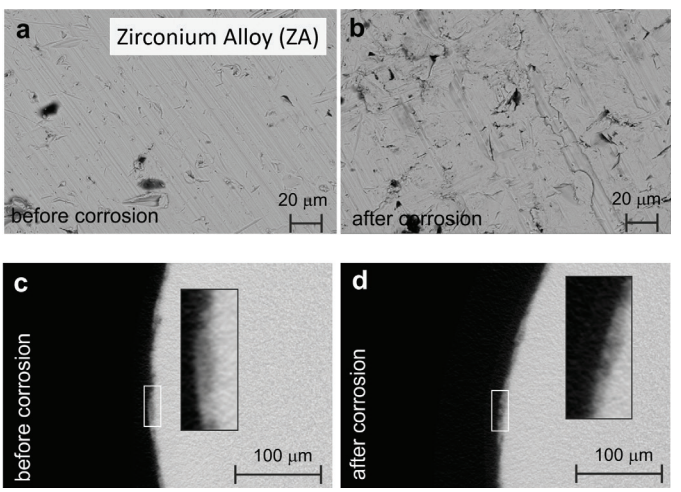

Figure 1: SEM (a,b) and X-ray microscope (c,d) investigation of the surfaces of ZA before (a,c) and after (b,d) exposition to bentonite B36.

The SEM and XRM results obtained for the spheroidal graphite cast iron (SGCI) before and after exposure to bentonite B36 are shown in Fig. 2. Before the test the surface showed the typical texture arisen from the cutting method and dark spots ascribed to the graphite spheres (Fig. 2a). After the corrosion test (Fig. 2b) a granular aspect can be observed with grain sizes of 20 – 50 µm. Those with a brighter appearance (indicated as Fe) could be identified by EDX as non-dissolved cementite (Fe_3C). Grains with a grey appearance (FeSiAl) showed a composition of (at%): Si: 8.9, O: 47.1, Fe: 21.2 and Al: 4.1. Subtracting the composition for bentonite (at%): Si: 8.9, O: 23.58, Al: 0.9, and Fe: 2.9, it remains a at% Fe/O ratio of ~ 1.15, suggesting the reaction of iron with bentonite to form an iron-rich silicate (with Fe either in the lattice or interlayer). Silicates remained sticked on the surface after rinsing and are supposed to be intimately intergrown with the less corroded Fe-grains. EDX results, therefore, could be used only qualitatively. The grains with a black appearance could be ascribed to the graphite particles. Note that they appear larger after corrosion, implying the dissolution of the partial iron cover formed during the cutting process.

The XRM picture in Fig. 2c representing the surface before corrosion showed a rough fringe indicating the roughen topography of the pellet side wall. After the corrosion test, the surface periphery indicated an undermining of the surface by metal dissolution leaving slightly attacked grains, grains of iron-aluminum-silicates, and a partial exposure of the graphite particles. An average corrosion layer of 10 µm could be measured.

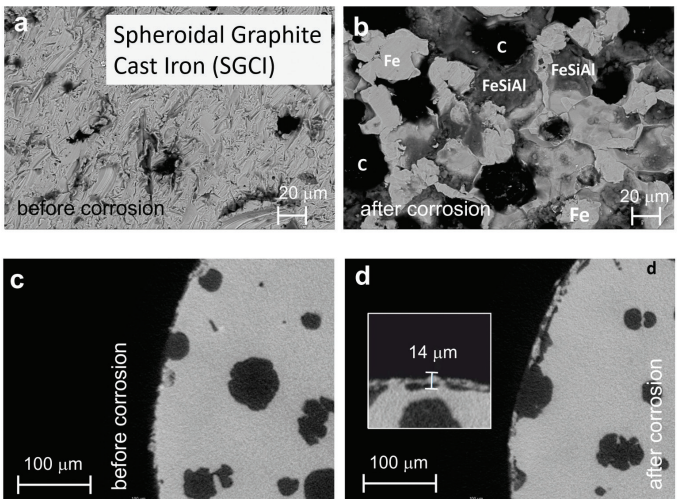

Figure 2: SEM (a,b) and X-ray microscope (c,d) investigation of the surfaces of SGCI before (a,c) and after (b,d) exposition to bentonite B36.

Fig. 3 shows the results of SEM and XRM investigations of corroded (b,d) and uncorroded (a,c) spring steel (SS). In contrast to the previously analyzed cast iron (SGCI), the surface of SS was covered by gel like deposits already before the corrosion experiment (Fig. 3a). These present a dark grey appearance and extent with a ramified shape over a background structure, characterized by grey filigree on a brighter matrix. From the picture, it seems that this corrosion product grows preferentially

on the grey ribbons of the underlying structure. Similar structures were described by Kaufhold et al.[9] and attributed to formation of ferrous hydroxide gel which upon exposure to air can further be oxidized to hematite with its characteristic red color; anaerobically hydroxide converts into magnetite. Such jelly structures readily form as Fe-rich materials are exposed to moisture. The starting sample also shows parallel oriented strips which were caused by production of the pellet, similarly, as observed for ZA (Fig. 1). After the corrosion test, a grained structure constituted of woodchips like particles of 3-5 µm with a bright aspect mixed with grey, gel-like precipitates can be observed (Fig. 3b), similar as for SGCI. The former may be goethite based on comparing their typical crystal morphology[40] and their composition of (at%) Fe:33, O: 66. The grey precipitates can be ascribed to iron-rich silicates. The XRM picture of the surface before corrosion shows - as in the previous cases - an irregular but well-defined periphery. The corresponding picture taken after corrosion clearly shows the advance of the metal dissolution front leaving a particulate layer with a thickness varying between 10 µm and 20 µm.

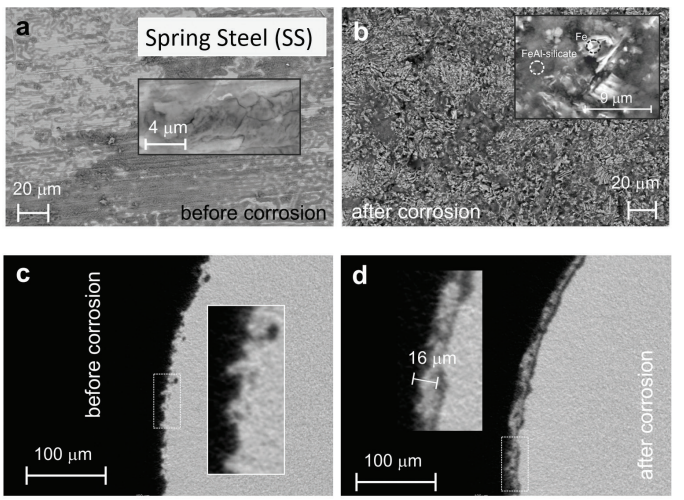

Figure 3: SEM (a,b) and X-ray microscope (c,d) investigation of the surfaces of SS before (a,c) and after (b,d) exposition to bentonite B36.

The surface of the CuNi alloy (CNA) before the corrosion test showed a bright aspect with the typical topography arising from the EDW-cutting (electrical discharge wire-cutting) process: scratches and pits generated by the dielectric discharge (see Fig. 4a). After the corrosion test, a structure constituted by grains with different stages of attack could be distinguished. In general, the bright appearance transforms in a rather matte one. A selective dissolution type seems to have taken place in the attacked grains (see Fig.4b). EDX performed inside the craters (see magnification at the up-right corner) allowed identifying the sticking of bentonite and some Al and Fe oxides on the corroding surface. EDX analyses performed at different points of the surface indicate variations of at% Cu/Ni ratio of 4-16 > 2 (substrate), confirming the preferential dissolution of Ni. Comparing the periphery of the cross-sectional XRM images before and after corrosion (Fig. 4a and b, respectively), it is evident that different grains are subject to different levels of corrosion attack. This is demonstrated by the appearance of a conspecific pattern on the sample surface, indicating the orientation dependence of metal dissolution.

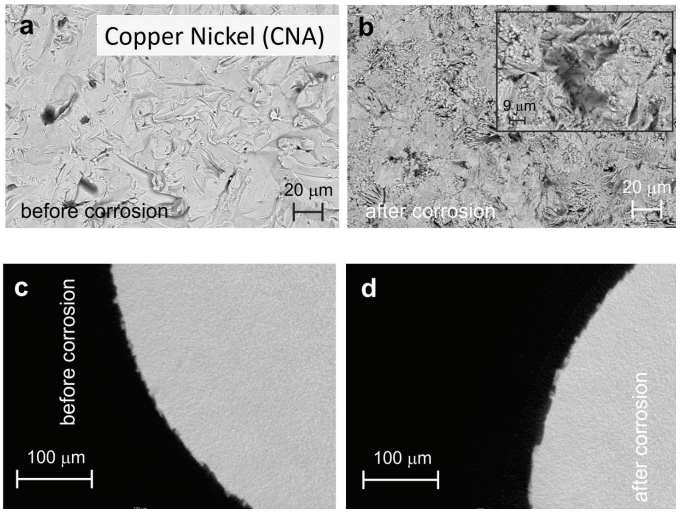

Figure 4: SEM (a,b) and X-ray microscope (c,d) investigation of the surfaces of CNA before (a,c) and after (b,d) exposition to bentonite B36.

Before the corrosion test, the surface of fine-grained construction steel (FGCS) was covered by irregular spots constituted by jelly structures resembling coral reefs similar as found on the surface of SS (see fig.5a). After the corrosion test (fig.5b), the natural iron oxide layer covering the initial surface disappears and a granular structure is formed, which results from the differentiated, orientation-dependent dissolution of the grains at the interface with the corrosive environment. The space left between particles of apparently slightly corroded grains composed predominantly of iron are filled with iron-aluminum-silicates sticking on the corroded surface. As in the case of SGCI and SS, the corrosion process under anaerobic conditions enables the development of the metallurgic structure, as a kind of etching procedure. The differentiated dissolution rate of grains leads to the development of a granulate structure composed of iron as major element. The largest Fe grains were

found on the surface of SGCI, followed by FGCS. By far the finest Fe grains were found on the surface of SS.

Using XRM, a nicely developed corrosion layer was observed on the cross-section of fine-grained construction steel (FGCS) (see Fig. 5d) with a thickness ranging from 5-15 µm. Often brighter particles were observed at the outside of the corrosion layer and darker (lighter) particles were found at the inner side of the layer. To obtain more information about the structure of the corroded surface, SEM pictures were taken at an angular direction to see the periphery of the button sample in more detail (see Fig. 6). The brighter, denser particles are almost embedded in a conglomerate of darker, lighter particles. The former could be identified by means of EDX as partially oxidized metallic particles constituted by Fe, Cu and Zn. The latter correspond to iron-aluminum-silicates.

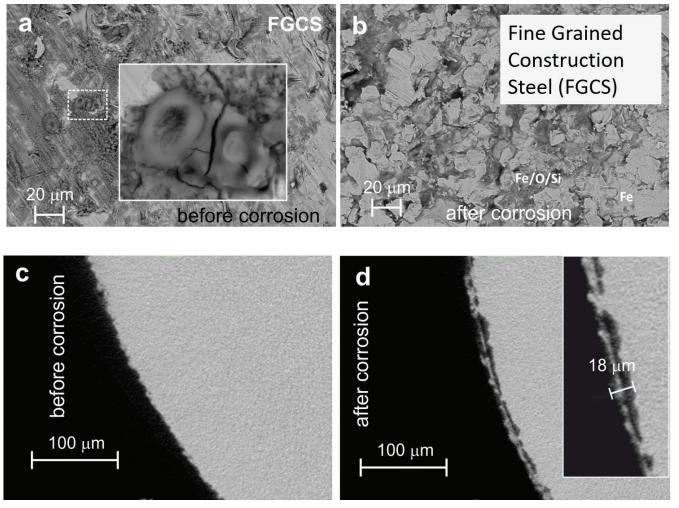

Figure 5: SEM (a,b) and X-ray microscope (c,d) investigation of the surfaces of FGCS before (a,c) and after (b,d) exposition to bentonite B36.

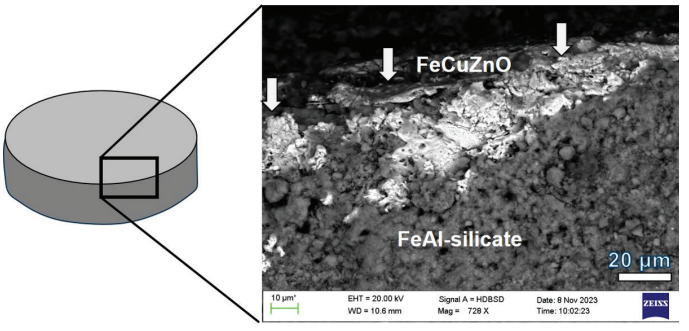

Figure 6: SEM image of the edge of the corroded FGCS pellet. Arrows point to areas in which the denser material (Fe-oxyhydroxide including some Cu and Zn) is lying on top of the corrosion layer.

Fig. 7a and b show the surface of the austenitic stainless steel (ASS) pellets before and after the corrosion test, respectively. The starting surface shows many scratches and pits, characteristic for an EDW-cutting method (like ZA). Comparing both pictures, a and b, it can be inferred that the corrosion test increased the roughness of the original surface by an attack occurring preferentially at defects points: as a consequence, an enlargement of craters and scratches occurs. This indicates that certain attack occurs initially on the surface, but it stops after a certain point, probably because of the formation of a stable passivation layer. The XRM-pictures before and after the corrosion test indicated that the initially rough fringe of the pellets turns rougher (compare Fig. 7c and d). This indicates that the dissolution process only progresses for a very short time until a completely passivating barrier is formed by oxide layer formation and reaction with the bentonite.

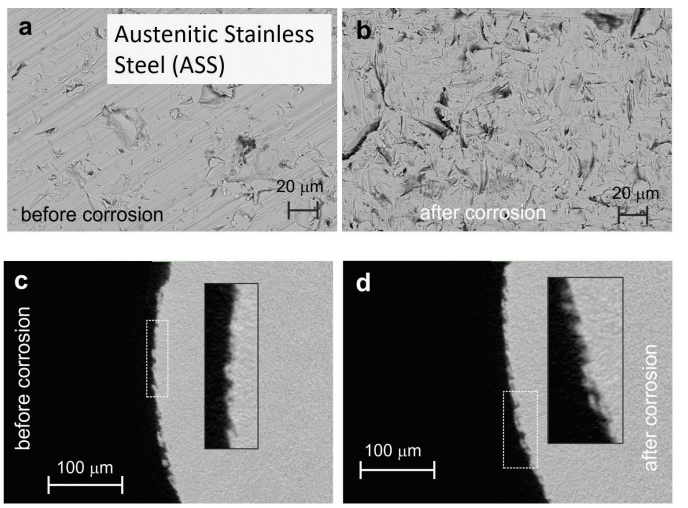

Figure 7: SEM (a,b) and X-ray microscope (c,d) investigation of ASS before (a,c) and after (b,d) exposition to bentonite B36.

Discussion

After the corrosion tests, the three selected metals with a predominating iron matrix (low alloyed Fe-based materials: SGCI, SS, FGCS; Table 2) showed a characteristic coating layer consisting of a conglomerate of particles with dark and bright appearance in the SEM pictures. The particles with a bright aspect can be associated to the non-corroded parts of the native iron matrix which are not covered with iron oxyhydroxide, as supported by the low oxygen content measured by EDX. The space among them corresponds to the cavities which are either empty or filled with iron-aluminosilicates.

From the mass loss measurements and the dimensions of the pellets, a mean corrosion rate given as µm per year was calculated. This value, however, should be taken with caution in the light of the microstructure of the observed corrosion layer. The morphological characterization has shown that there is a differentiated metal dissolution rate influenced by the crystallographic phases and their grain orientations. This leads to a non-uniform corrosion in the microscale. This aspect was also pointed out by Hesketh et al.[23], who reported the formation a non-continuous film consisting of a mixture of iron oxides (magnetite and oxyhydroxides) and bentonite/silicates adhering to the surface of carbon steel (C < 0.20 % w/w). The corrosion layer reached a thickness of up to some tens of microns at some points of the sample in ex-situ experiments using long pieces of thin carbon steel wires.

The effects of the crystallographic orientation on the dissolution and passivation of pure iron were investigated by Schreiber et al.[41] on a polycrystalline material using a capillary cell. The (101) orientation, for instance, shows a Flade-current (active-passive transition) more than twice of that required for the (100) face. The grain boundaries, on the other hand, can act as highly active corrosion sites as natural consequence of the more stressed crystal structure. Thus, steels with finer grains are susceptible to a higher corrosion[42,43]. This tendency, however, could be inverted if the dissolved iron contributes to the formation of a passivating film by reaction with the contact media.

The use of mechanically untreated surfaces in this study aims a more realistic scenario. The irregular distributed stressed metal facets exposed with their different grain orientations and compositions together with their partial coverage with a passive film provides a mean value of the corrosion rate. The materials used in this study correspond to the industrial standard and are considered representative of the application. No attempt was made to achieve a specific grain orientation either by sample preparation or processing. The results therefore correspond to the average of all grains exposed to the surface. Thus, the corrosion rate values calculated from mass loss measurements are more reliable for long-term assessments. Some minor errors, however, can be introduced, for instance, by adhered iron-aluminosilicates found after the corrosion test even after intense washing of samples. Thus, the retention of dissolved iron in low density corrosion products could lead to misleading results. In the case of the iron-matrix materials SGCI, SS, and FGCS the thickness of the corrosion layers measured on XRM-pictures exceeded those determined gravimetrically by 10-50 %. Evidently, i) it is because some grains were much less affected by corrosion and hence did not corrode and ii) because of the presence of iron-aluminosilicates which represent an added mass to the surface.

Apart from these issues, the corrosion rates measured after ten months should represent the very initial corrosion stages considering the more than three order of magnitude longer periods regarded in long-term assessments. These values, on the other hand, would be overestimated in view of the time exponential decay found by Hesketh et al.[23] in about ten years long experiments. The present corrosion study, however, was designed as a reliable test for the selection of a material among different options.

Gravimetrically, no corrosion could be measured for ZA. After the exposition test, however, the surface morphology changed in a way that the initial scratch pattern produced by cutting can be only partially discerned. It seems like patches of a film would cover the original substrate. It is known that Zr forms an insulating ZrO2 film in contact with water of up to 4 µm thickness which hinders further corrosion[44]. A possible explanation for these microscopic changes is the growth of a protective oxide initiated in the more defect regions together with a simultaneous very slow dissolution, thus compensating for the mass gain caused by the oxide. No detectable mass changes in the test length let classify this material as practically inert.

For SGCI, an iron matrix alloy containing ferrite, pearlite, and graphite spheres, a corrosion layer of about 10 µm thickness was observed (see Fig.2d). This consists of grains of unreacted iron phases and voids which were filled by iron-aluminosilicates. The graphite particles do not react with the bentonite and are gradually exposed by dissolution of the surrounding iron phases probably because the graphite serves as cathodic site.

In the case of SS, the corrosion reveals its metallographic structure. The rapid quenched low carbon steel is constituted by a mixture of fine grains of ferrite combined with Fe,Si carbide precipitates due to the high silicon content. In some cases, graphite is precipitated as so-called temper coal due to the reduction in carbon solubility caused by the alloying element silicon (see fig.3b). The more rapid dissolution of ferrite leaves a corrosion layer constituted by slower dissolving martensite and iron-aluminosilicates arising from the reaction of dissolved iron with the bentonite[45]. Thus, the very different morphologies of the corrosion layer observed for SGCI and SS is the result of the different iron phases present and their size distribution. The fine

grain distribution of the SS allows a more even advance of the corrosion front.

Even though the grain sizes of SGCI and SS differed by about one order of magnitude, similar corrosion rates and thicknesses of the corrosion layer were found. Probably, this is evidence for a corrosion process controlled by diffusion process, e.g., by the outward diffusion of Fe2+ and/or H2 into the bentonite.

The corroded surface of CNA shows a considerable increase of the surface roughness, also characterized by localized dissolution which leaves a sand-like structure. The corroded surface appears decorated with particles smaller than 1 µm which could be ascribed to a redeposition of Cu[46]. The selective dissolution of the less noble Ni leads to some mass loss which can be counted as a corrosion rate of 1 µm/a. The presence of some Si containing particles on the surface indicates the formation of a corrosion product by interaction of dissolved nickel with the bentonite. This material, therefore, cannot be considered inert but much more resistant towards corrosion in comparison with the iron matrix alloys SGCI and SS.

The corrosion of FGCS, shows some similarities to that observed with SGCI and SS. As in the case of SS, the gel-like corrosion products formed before the corrosion test disappeared completely after the experiment. A morphology characterized by the dissolution of more active grains (ferrite) and the formation of iron-aluminosilicates filling the voids can be observed, similarly as after the corrosion of SGCI. The thickness of the corrosion layer varies between 10 µm and up to 20 µm. The corrosion layer of this material clearly shows a dark grey layer closest to the pristine metal surface followed by a variable brighter layer. With the XRM only two grey scales were identified but SEM suggests the presence of more phases of different density. Therefore, it is not clear if the darker inner layer corresponds to Fe-silicates or Fe-oxyhydroxides. SEM pictures taken from the edge of a pellet (see Fig.6) indicate that the outermost particles are Fe-oxyhydroxides lying on top of the iron-aluminosilicate layer. It remains speculative if the observed oxide layer was formed on the surface before the corrosion test and displaced outwards by the formation of silicates or a mixing of oxyhydroxides and silicates was formed.

The surface of ASS showed an enlargement of craters and scratches which indicates that certain attack occurs initially on the surface, but it stops after a certain point, probably because of the formation of a stable passivation layer. Gravimetrically, however, no mass loss could be determined which suggests that ASS did not react with the bentonite.

Conclusions

The corrosion of six metallic materials in contact with bentonite under anaerobic conditions were tested. The gravimetrical results were in accordance with electron and X-ray optical data in that a corrosion layer was found for those materials which showed significant mass loss. All Fe-rich alloys (Fe > 90 mass%) showed corrosions rates around 10 µm/a after 10 months and hence are more reactive compared to the others. The surface of the Fe-rich materials did not corrode uniformly. The corrosion layer consists of iron phases and voids caused by corrosion of ferrite phases which were filled by the formed iron-aluminosilicates. The corrosion rates of these three iron-rich materials were similar and not significantly affected by different grain size, previous state of the exposed surface, and/or the presence or absence of graphite particles. Minor corrosion was found for the CuNi-alloy CNA but it was negligible for the Zr-based alloy ZA and the stainless steel ASS. The results suggest that these latter two materials are undoubtedly advantageous compared to carbon steels with respect to corrosion resistance in contact with bentonite. Therefore, further investigations of the long-term performance of the passive layer of stainless steel and zirconium under as realistic near field disposal conditions as possible (not only using solutions), should be pursued.

Acknowledgements

The Federal Ministry for Environment, Nature Conservation, Nuclear Safety and Consumer Protection (BMUV; grant no. 02 E 11981A-C) are gratefully acknowledged for the funding of this work.

Stephan Kaufhold is a research scientist at BGR (Hannover, Germany) with a PhD in mineralogy. He focuses on reactions of clay minerals particularly in the field of radioactive waste management.

Christoph Kahra is a research scientist at the Leipniz university Hannover with a M. Sc. in mechanical engineering. His research areas include heat treatment, fatigue and X-ray microscopy.

Nicolas Finck is a research scientist at KIT with a PhD in radiochemistry. His research focuses on the formation of secondary phases and their affinity for radionuclides uptake in the context of nuclear waste disposal.

Thomas Hassel is head of the Hannover Underwater Technology Center (UWTH) at the Institut für Werkstoffkunde (Materials Science) at Leibniz University Hanover (Germany). His research areas range from final storage container technology,

welding and cutting technologies to the corrosion of welded metal joints.

Andrés G. Muñoz is a research and development scientist at GRS (Germany) with a PhD in Materials Science. He is dedicated to solving fundamental and applied surface (photo)-electrochemistry issues on metal corrosion and passivity, metal coatings, and semiconductors.

References

1. Bel, J.J.P., Wickham, S.M., Gens, R.M.F. 2006. Development of the Supercontainer Design for Deep Geological Disposal of High-Level Heat Emitting Radioactive Waste in Belgium. *MRS Online Proceedings Library 932*: 1221. https://doi.org/10.1557/PROC-932-122.1
2. Verhoeven, B., Bogaerts,W., Van Aken, P., Gaggiano, R., Baeyens, J., Rossi, B., Dewil, R. 2022. Pitting and General Corrosion Susceptibilities of Materials for High Level Radioactive Waste (HLW) Disposal. *Materials* 15: 6464. https://doi.org/10.3390/ma15186464
3. Sellin, P., Leupin, O. X. 2013. The Use of Clay as an Engineered Barrier in Radioactive-Waste Management − A Review. *Clays Clay Minerals* 61: 477–498.
4. Carlsson, T., Muurinen, A. 2007. *Copper corrosion in bentonite: Studying parameters (pH, Eh/O2) of importance for Cu corrosion.* Posiva. Working report 2007-62.
5. Kosec, T., Qin, Z., Chen, J. 2015. Copper corrosion in bentonite/saline groundwater solution: effects of solution and bentonite chemistry. *Corrosion Science 90:* 248–258.
6. Stoulil, J., Horácková, L., Rihová-Ambrozova, J. 2014. Corrosion behavior of copper in wet bentonite Rokle B75. *Koroze a ochrana materiálu.* 2014: 58:43–47.
7. Kaufhold, S., Dohrmann, R., Gröger-Trampe, J. 2017. Reaction of native copper in contact with pyrite and bentonite in anaerobic water at elevated temperature. *Corrosion Engineering Science and Technology 52:* 349 – 358.
8. Wersin, P., Kober, F. 2017. FEBEX-DP Metal Corrosion and Iron-Bentonite Interaction Studies. Nagra Arbeitsberichte NAB 16-16, NAGRA Wettingen Switzerland, p. 300.
9. Kaufhold, S., Schippers, A., Marx, A., Dohrmann, R. 2020. SEM study of the early stages of Fe-bentonite corrosion—The role of naturally present reactive silica. *Corrosion Science 171:* 108716.
10. Hadi, J., Wersin, P., Jenni, A., Greneche, J.M. 2017. Redox Evolution and Fe-Bentonite Interaction in the ABM2 Experiment, Äspö Hard Rock Laboratory. NTB--17-10 NAGRA Wettingen Switzerland, p. 330.
11. Wilson, J.C., Benbow, S., Sasamoto, H., Savage, D., Watson, C. 2015. Thermodynamic and Fully-Coupled Reactive Transport Models of a Steel-Bentonite Interface. *Applied Geochemistry 61:* 10–28, doi:10.1016/j.apgeo-732 chem.2015.05.005.
12. Xia, X., Idemitsu, K., Arima, T., Inagaki, Y., Ishidera, T., Kurosawa, S., Iijima, K., Sato, H. 2005. Corrosion of Carbon Steel in Compacted Bentonite and Its Effect on Neptunium Diffusion under Reducing Condition. *Applied Clay Science 28:* 89–100, doi:10.1016/j.clay.2004.01.002.
13. Soltermann, D., Fernandes, M. M., Baeyens, B., Dahn, R., Joshi, P. A., Scheinost, A. C., Gorski, C. A. 2014. Fe(II) Uptake on Natural Montmorillonites. I. Macroscopic and Spectroscopic Characterization. *Environmental Science and Technology 48:* 8688, dx.doi.org/10.1021/es501887q
14. Kaufhold, S., Dohrmann, R., Ufer, K., Kober, F. 2018. Interactions of bentonite with metal and concrete from the FEBEX experiment - mineralogical and geochemical investigations of selected sampling sites. ***Clay Minerals 53:*** 745–763.
15. Lantenois, S., Lanson, B., Muller, F., Bauer, A., Jullien, M., Plançon, A. 2005. Experimental study of smectite interaction with metal Fe at low temperature: 1. Smectite destabilization. *Clays Clay Minerals 53:* 597–612.
16. Lanson, B., Lantenois, S., van Aken, P. A., Bauer, A., Plançon, A. 2012. Experimental investigation of smectite interaction with metal iron at 80°C: Structural characterization of newly formed Fe-rich phyllosilicates. *American Mineralogist 97:* 864–871.
17. Pignatelli, I., Mugnaioli, E., Hybler, J. 2013. A Multi-Technique Characterization of Cronstedtite Synthesized by Iron-Clay Interaction in a Step-By-Step Cooling Procedure. *Clays Clay Minerals 61:* 277–289. https://doi.org/10.1346/CCMN.2013.0610408
18. Kaufhold, S., Klimke, S., Schlömer, S., Alpermann, T., Renz, F., Dohrmann, R. 2020. About the corrosion mechanism of metal iron in contact with bentonite. *ACS Earth and Space Chemistry 4:* 711 – 721. doi.org/10.1021/acsearthspacechem.0c00005.
19. Foct, F., Gras, J.M. 2002. Semi-empirical model for carbon steel corrosion in long term geological nuclear waste disposal, Proceedings of the International Workshop Prediction of Long Term Corrosion Behaviour in Nuclear Waste Systems, Cadarache, France, 2002.
20. Stoulil, J., Kanok, J., Kouril, M., Parschova, H., Novak, P. 2013. Influence of temperature on corrosion rate and porosity of corrosion products of carbon steel in anoxic bentonite environment, *J. Nucl. Mater. 443:* 20–25.
21. Smart, N. R., Reddy, B., Rance, A. P., Nixon, D. J., Diomidis, N. 2017. The anaerobic corrosion of carbon steel in saturated compacted bentonite in the Swiss repository concept. *Corrosion Engineering, Science and Technology 52:* 113–126.
22. King, F. 2013. Container Materials for the Storage and Disposal of Nuclear Waste. *Corrosion 69*: 986-1011. doi.org/10.5006/0894
23. Hesketh, J., Haynes, H., Reddy, B., Rance, A., Bevas, C., Padovani, C., Diomidis, N. 2023. *Mater. Corros. 74:* 1728–1745. https://doi.org/10.1002/maco.202313767
24. Kaufhold, S., Sanders, D., Dohrmann, R., Hassel, A.-W. 2015. Fe corrosion in contact with bentonites. *Journal of Hazardous Materials 285:* 464–473.

25. Cramer, S.D., Covino, B.S. (Eds.). 2005. ASM Handbook, Vol.13B Corrosion: Materials, ASM International, Ohio.
26. Szklarska-Smialowska, Z. 2005. Pitting and Crevice Corrosion, NACE International, Houston, TX. 88.
27. Caluscio Dos Santos, D., Monfrinatti Macarrão, I., Magnabosco, R. 2020. Relation between pitting potential and PREN values for ferrite and austenite in duplex stainless steels. *BHM Berg-und Hüttenmännische Monatshefte 165:* 46-50.
28. Wu, X., Liu, Y., Sun, Y., Dai, N., Li, J., Jiang, Y. 2021. A discussion on evaluation criteria for crevice corrosion of various stainless steels. *Journal of Materials Science & Technology 64:* 29-37.
29. Payer, J.H., Finsterle, S., Apps, J.A., Muller, R.A. 2019. Corrosion Performance of Engineered Barrier System in Deep Horizontal Drillholes. *Energies 12:* 1491. https://doi.org/10.3390/en12081491
30. Stoulil, J., Pavlova, L., Kouril, M. 2019. Localised corrosion of stainless steels 316L and 2205 in synthetic bentonite pore water and bentonite slurry. *Acta Metallurgica Slovaca 25:* 24-32. doi.org/10.36547/ams.25.1.4
31. Reddy, B., Padovani, C., Rance, A.P., Smart, N.R., Cook, A., Haynes, H.M., Milodowski, A.E., Field, L.P., Kemp, S.J., Martin, A.J., Diomidis, N. 2020. The anaerobic corrosion of candidate disposal canister materials in compacted bentonite exposed to natural granitic porewater containing native microbial populations. *Materials and Corrosion:* 1 – 22. https://doi.org/10.1002/maco.202011798
32. Gaudin, A., Gaboreau, S., Tinseau, E., Bartier, D., Petit, S., Grauby, O., Foct, F., Beaufort, D. 2009. Mineralogical reactions in the Tournemire argillite after in-situ interaction with steels, *Applied Clay Science 43:* 196-207, https://doi.org/10.1016/j.clay.2008.08.007.
33. Necib, S., Schlegel, M. L., Bataillon, C., Daumas, S., Diomidis, N., Keech, P., Crusset, D. 2019. Long-term corrosion behaviour of carbon steel and stainless steel in Opalinus clay: influence of stepwise temperature increase. *Corrosion Engineering, Science and Technology, 54:* 516–528. https://doi.org/10.1080/1478422X.2019.1621456
34. Tholen, M. 2009. Chemisch-toxische Stoffe in einem Endlager für hochradioaktive Abfälle. APII – Inventar chemotoxische Stoffe. DBE Technology GmbH, Peine.
35. Gao, X., Liu, M. 2022. Corrosion behavior of high-strength C71500 copper-nickel alloy in simulated seawater with high concentration of sulfide. *Materials 15:* 8513.
36. Guo, X., Gin, S., Liu, H., Ngo, D., Luo, J., Kim, S. H., Frankel, G. S. 2020. Near-field corrosion interactions between glass and corrosion resistant alloys. *Npj Materials Degradation 4:* 10.
37. Kaufhold, S., Hein, M., Dohrmann, R., Ufer, K. 2012. Quantification of the mineralogical composition of clays using FTIR spectroscopy. *Journal of Vibrational Spectroscopy 59:* 29 - 39.
38. Prathipati, R., Ch, R., Dora, S.P. 2019. Corrosion behavior of surface induced by wire EDM on 316L stainless steel: an experimental investigation. *SN Appl. Sci.* 1: 952. https://doi.org/10.1007/s42452-019-0992-4
39. Sidhom, H. Habib, Ghanem, F., Amadou, T., Gonzalez, G., Braham, Ch. 2013. Effect of electro discharge machining (EDM) on the AISI316L SS white layer microstructure and corrosion resistance. *International Journal of Advanced Manufacturing Technology 65:* 141-153
40. Montes-Hernandez, G., Beck, P., Renard, F., Quirico, E., Lanson, B., Chiriac, R., Findling, N. 2011. Fast precipitation of acicular goethite from ferric hydroxide gel under moderate temperature (30 and 70 °C). *Cryst. Growth Des. 11:* 2264–2272.
41. Schreiber, A., Schultze, J.W., Lohrengel, M.M., Kármán, F., Kálmán,E. 2006. Grain dependent electrochemical investigations on pure iron in acetate buffer pH 6.0. *Electrochimica Acta 51:* 2625-2630. https://doi.org/10.1016/j.electacta.2005.07.052.
42. Rai, P.K., Shekhar, S., Mondal, K. 2018. Development of gradient microstructure in mild steel and grain size dependence of its electrochemical response. *Corrosion Science 138:* 85-95. https://doi.org/10.1016/j.corsci.2018.04.009.
43. Wang, P., Ma, L., Cheng, X., Li, X. 2021. Effect of grain size and crystallographic orientation on the corrosion behaviors of low alloy steel, *J. Alloy Compounds 857:* 158258.
44. Shoesmith, D.W., Zagidulin, D. 2011. The corrosion of zirconium under deep geologic repository conditions, *J. Nucl. Mater. 418:* 292-306.
45. Chen, H., Lv, Z., Lu, L., Huang, Y., Li, X. 2021. Correlation of micro-galvanic corrosion behavior with corrosion rate in the initial corrosion process of dual phase steel, *J. Mater. Res. Tech. 15:* 3310-3320.
46. Beccaria, A.-M., Crousier,J. 1989. Dealloying of Cu-Ni alloys in natural see water, *Br. Corros. J. 24:* 49-52.